

Article

Ultraviolet Camera Measurements of Passive and Explosive (Strombolian) Sulphur Dioxide Emissions at Yasur Volcano, Vanuatu

Tehnuka Ilanko ¹, Tom D Pering ^{1,*}, Thomas Charles Wilkes ¹, Julia Woitischek ^{2,3}, Roberto D'Aleo ⁴, Alessandro Aiuppa ⁵, Andrew J S McGonigle ^{1,6,7}, Marie Edmonds ² and Esline Garaebiti ⁸

- ¹ Department of Geography, University of Sheffield, Winter Street, Sheffield S10 2TN, UK; t.ilanko@sheffield.ac.uk (T.I.); tcwilkes1@sheffield.ac.uk (T.C.W.); a.mcgonigle@sheffield.ac.uk (A.J.S.M.)
- ² Department of Earth Sciences, University of Cambridge, Downing Street, Cambridge CB2 3EQ, UK; jw943@cam.ac.uk (J.W.); me201@cam.ac.uk (M.E.)
- ³ BP Institute, University of Cambridge, Madingley Rd, Cambridge CB3 0EZ, UK
- ⁴ INGV, Sezione di Palermo, Via Ugo la Malfa 153, 90146 Palermo, Italy; roberto.daleo01@unipa.it
- ⁵ DiSTeM, Università di Palermo, Via Archirafi, 22, 90123 Palermo, Italy; alessandro.aiuppa@unipa.it
- ⁶ School of Geosciences, the University of Sydney, Sydney 2006, Australia
- ⁷ Faculty of Health, Engineering and Sciences, University of Southern Queensland, Toowoomba 4350, Australia
- ⁸ Geohazards Division, Vanuatu Meteorology and Geo-hazards Department, Lini Highway, Port Vila, Vanuatu; gesline@vanuatu.gov.vu
- * Correspondence: t.pering@sheffield.ac.uk

Received: 29 June 2020; Accepted: 17 August 2020; Published: 20 August 2020



Abstract: Here, we present the first ultraviolet (UV) camera measurements of sulphur dioxide (SO₂) flux from Yasur volcano, Vanuatu, for the period 6–9 July 2018. These data yield the first direct gas-measurement-derived calculations of explosion gas masses at Yasur. Yasur typically exhibits persistent passive gas release interspersed with frequent Strombolian explosions. We used compact forms of the “PiCam” Raspberry Pi UV camera system powered through solar panels to collect images. Our daily median SO₂ fluxes ranged from 4 to 5.1 kg s⁻¹, with a measurement uncertainty of −12.2% to +14.7%, including errors from the gas cell calibration drift, uncertainties in plume direction and distance, and errors from the plume velocity. This work highlights the use of particle image velocimetry (PIV) for plume velocity determination, which was preferred over the typically used cross-correlation and optical flow methods because of the ability to function over a variety of plume conditions. We calculated SO₂ masses for Strombolian explosions ranging 8–81 kg (mean of 32 kg), which to our knowledge is the first budget of explosive gas masses from this target. Through the use of a simple statistical measure using the moving minimum, we estimated that passive degassing is the dominant mode of gas emission at Yasur, supplying an average of ~69% of the total gas released. Our work further highlights the utility of UV camera measurements in volcanology, and particularly the benefit of the multiple camera approach in error characterisation. This work also adds to our inventory of gas-based data, which can be used to characterise the spectrum of Strombolian activity across the globe.

Keywords: sulphur dioxide; remote sensing; ultraviolet cameras; Strombolian explosions

1. Introduction

Strombolian volcanism is one of the more common forms of basaltic explosive activity globally, associated with the rapid ejection of hot pyroclasts from a vent in a single impulsive burst [1,2],

with event frequencies ranging from seconds to minutes [3]. Volcanoes with frequent Strombolian activity include the archetypal Stromboli, Italy [4,5]; Pacaya, Guatemala [6,7]; Erebus, Antarctica [8–11]; and Yasur, Vanuatu [12–14], the subject of this study. Other volcanoes also known to produce Strombolian activity include Etna, Italy [15–17]; Villarrica, Chile [18]; Arenal, Costa Rica [19,20]; Batu Tara, Indonesia [21,22]; and Shishaldin, USA [23].

Classically, this style of behaviour has been related to the ascent from depth of elongated and overpressured bubbles, termed gas slugs (Taylor bubbles), which rapidly expand in length as they approach the surface [2,24–26]. However, recent research has suggested that the causal mechanisms may be far more diverse [27–30] and that the presence of crystal-rich layers in the magmatic column is important in the mechanism of Strombolian explosions. To test these hypotheses, it is useful to investigate the spectrum of Strombolian activity at volcanoes where this behaviour is typical, including Yasur. In addition, recent studies have highlighted the importance of the eruption frequency in determining the behaviour of ascending gas slugs [21], as well as interslug interactions [15,31]. This has led to the classification of behaviour styles, ranging from rapidly bursting slugs, which may interact with one another during ascent, through to single bursting slugs [3,31].

There are several methods used to obtain information about individual Strombolian explosions based on the capture of seismic [5,32], infrasonic [6,33–35], thermal [4,5], and gas-derived [15,36–38] data. Here, we focus on gas emission rate measurements using an ultraviolet (UV) camera, an instrument frequently used to quantify gas release from persistently outgassing volcanoes [39,40]. The UV camera is able to resolve rapid fluctuations in the release of sulphur dioxide (SO₂) gas. When the camera is used in tandem with an in situ multicomponent gas analyser (MultiGAS) to measure gas ratios within a volcanic plume [41,42], it is possible to estimate the total gas emission rate [43]. An important parameter with respect to causal mechanisms for Strombolian explosions is the ratio of gas released during explosions to that released passively [27,28,44–47]. This “active-to-passive” degassing ratio also provides information about conduit fluid dynamics [15,21,37,48]. For example, Tamburello et al. [38] discovered that the most efficient mode of degassing at Stromboli was actually the passive degassing, which accounted for ~77% of gases released, demonstrating the dominance of passive gas release [49] and the smaller gas bubbles within a volcanic conduit.

UV-camera-derived SO₂ masses from Strombolian explosions [15,34,38,50] can be combined with gas ratio data (e.g., from MultiGAS) to generate total gas masses and volumes for individual explosive events [15,51]. These data provide parameters for analytical and computational models of gas flow in conduits, which yield further information about the activity and mechanisms, for example on the slug length, explosive vigour, and categorisation of the burst behaviour using fluid dynamics [3,24,26,52].

Yasur Volcano

Yasur (Vanuatu) is a basaltic stratovolcano located on the southeast of Tanna Island, which is thought to have been persistently active for at least ~800 years [53]. The main volcanic edifice is a cone with a crater area measuring 350–450 m in diameter, divided by a septum into northern and southern craters, each containing multiple active vents exhibiting Strombolian-style behaviour. A number of studies on Yasur have focused on the characteristics of its Strombolian activity, particularly its dynamism. Multivent basaltic volcanoes are known to exhibit vent-specific behaviours that can change through time (e.g., at Stromboli) [30,54]. Simons et al. [55] discussed systematic changes in behaviour at individual vents within the southern crater at Yasur, showing switching from bomb-rich (incandescent pyroclasts) through to ash-rich explosions. They also discussed conduit branching and the possibility of a single bubble (i.e., gas slug) driving paired explosions from separate vents at Yasur, with the potential for eruption styles to diverge at different vents due to cooling of the magma in the upper conduit branches. Spina et al. [56] observed two decoupled styles of degassing from infrasound data: puffing, which was near-constant; and Strombolian explosions. Meier et al. [57] highlighted the ash-rich and ash-poor (or bomb-rich) styles and their similarity at Yasur to those of Stromboli [4,58–61].

Kremers et al. [12] were able to calculate the lengths of gas slugs generating the Strombolian explosions on Yasur as ranging from 59 to 244 m, with mean and median values of 112 m and 103 m, respectively.

SO₂ fluxes at Yasur ranged from 2.5 to 17.2 kg s⁻¹ from April 2004 to November 2005, with a mean of 7.9 kg s⁻¹ based on differential optical absorption spectroscopy (DOAS) traverses [13]. Between August 2007 and December 2008, SO₂ fluxes at Yasur were 1.3 to 11.1 kg s⁻¹, with a mean and median of 7.2 kg s⁻¹ and 7.1 kg s⁻¹, respectively [62]. In October 2007, a mean SO₂ flux of 8.0 ± 3.8 kg s⁻¹ across four days of traverses was reported [63]. A satellite-derived SO₂ flux of 6.8 to 23.3 kg s⁻¹ was estimated between 2000–2015, with a mean and median of 16.3 kg s⁻¹ and 19.2 kg s⁻¹, respectively [49]. Comparisons of gas flux between different periods of observations and between methods must be treated with caution; in discrete campaigns such as presented in this study, they may not represent broader changes through time.

Here, we demonstrate the use of a portable, solar-chargeable version of the low-cost Raspberry Pi ultraviolet camera [64,65] at Yasur, combined with a new approach to estimate plume velocity using UV camera imagery to obtain SO₂ fluxes. We present the first UV camera measurements at Yasur, providing gas-based estimates of explosive Strombolian gas masses, which are key to unravelling information on the spectrum of behaviours for this style of activity globally. Furthermore, we illustrate the use of statistical methods to differentiate between passive and explosive gas release, and finally apply mathematical models to estimate the driving slug dimensions of the Strombolian explosions at Yasur volcano.

2. Observed Activity during 5th to 11th July 2018

During the measurement period, an ashy plume was present throughout the week related to ash-rich Strombolian explosions arising from both craters (Figure 1). From the summit, multiple vents displaying incandescence were visible within the southern crater, each exhibiting different styles of explosive behaviour (Figure 1c). Gas release from the summit vents was constantly visible, occasionally including “puffing” (described elsewhere by [3,21,38,48]). The northern crater contained at least two vents, but access to its rim was precluded by safety concerns due to ballistic ejecta from the crater’s Strombolian explosions, which also appeared to be more ash-rich than those from the southern crater. From the southern crater (Figure 1d) we directly observed explosions from at least three vents. Each vent exhibited different behaviours, two with jet-like characteristics (i.e., with a strong vertical component to the trajectory of the ejecta), hinting at the potential influence of the conduit wall during the explosion process, i.e., the explosion (slug burst) happens deeper within the conduit, providing a vertical direction to the released material [66,67]. Another vent exhibited parabolic transport of incandescent pyroclasts (without an initial jet), as though an ascending bubble burst within an over-topped magma column [24] or within a flared conduit geometry [68], i.e., allowing the lateral expansion of bubble prior to burst. Interestingly, these Strombolian explosions also differed in the noise generated, with the hemispherical-shaped (non-jet-like) explosions associated with a deeper booming sound. During 8th to 9th July, explosions were frequently associated with visible shockwaves propagating through the condensed plume. Throughout the measurement period, the morphology of the crater was dynamic, with spatter and ash accumulating around vents leading to changes in the size, shape, and position of vents.

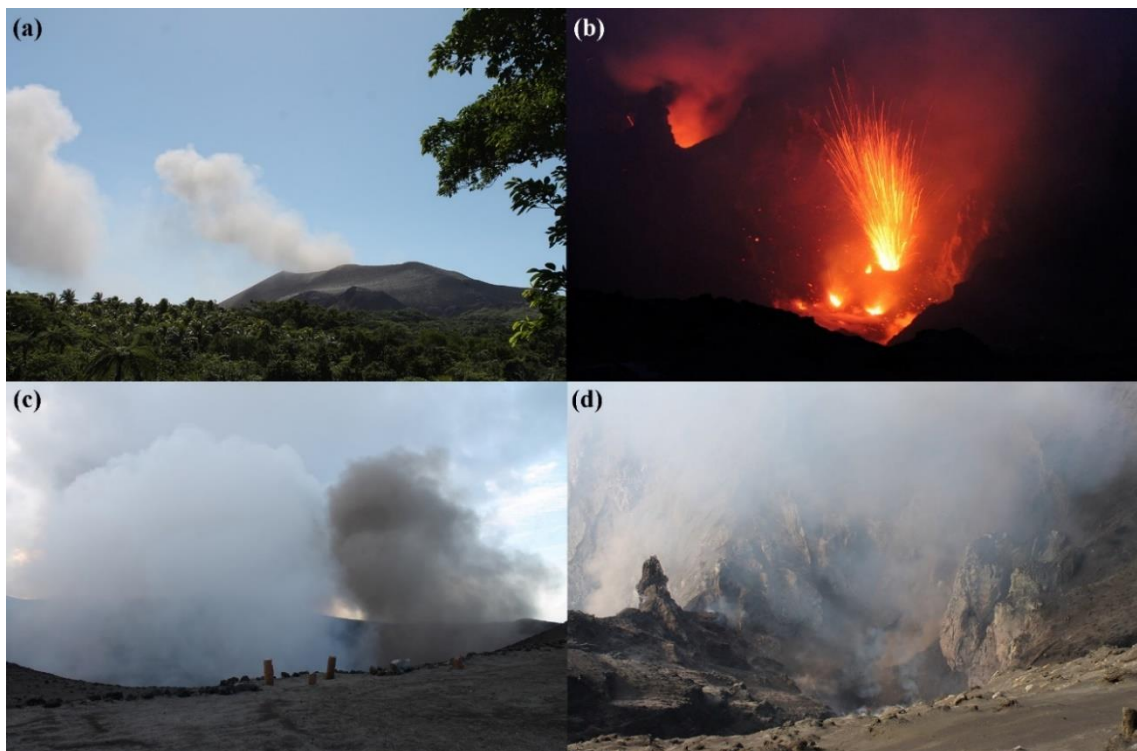


Figure 1. Activity at Yasur volcano, Vanuatu, during the July 2018 field campaign. (a) Image of the gas plume rising from the summit crater. Large gas pulses are associated with explosions. (b) A nighttime view, with the south crater in the foreground and incandescence from the north crater in the background. Several vents are visible in the south crater, with one producing a Strombolian explosion. (c) Ash-rich gas plumes formed by Strombolian explosions occurred from the north crater and ash-poor gas plumes from explosions from the south crater. (d) A daytime view into the north crater, showing the crater floor topography divided by a septum into northern and southern craters.

3. UV Camera Methods

Low-cost Raspberry Pi ultraviolet (UV) camera systems (PiCams) were used to measure volcanic SO_2 outgassing [64,65]. In this case the units were modified to include “PiJuice” hardware and software (<https://github.com/PiSupply/PiJuice>) to provide power to the Raspberry Pi boards at the heart of the camera system (see also [30]). The PiJuice units provide continuous supplies of power via lithium-polymer mobile phone batteries, which can be recharged using solar panels. In the field, both 1600 mAh and 2300 mAh batteries were used. With continuous solar charging (via 40 W solar panels for each Pi board), this configuration readily enabled field data acquisition for at least 6–7 h per day in this location. This camera setup omitted the GPS module used in the prior generation of the PiCam system, which automatically provided time synchronisation for the Raspberry Pi computers on start-up. Instead, GPS time synchronisation was performed manually via the command line, expedited by the PiJuices’ on-board real-time clocks. The PiCam systems were equipped with two Edmund Optics Inc. filters (full width at half maximum—10 nm), one for each lens, centred at around 310 and 330 nm, respectively, corresponding to spectral regions where SO_2 does and does not absorb incident UV radiation. As detailed further elsewhere, UV imaging systems in volcanic gas monitoring are predicated upon contrasting image intensities in these two wavebands in order to isolate absorption in the image cause by sulphur dioxide absorption; for further details please see [39,69–73].

Two separate PiCams (Camera 1 and Camera 2) were operated simultaneously (enabling assessment of error and comparison of two plume angles), viewing the plume from a position southwest of the summit crater from the treehouse site (~1900 m from the plume) at the jungle oasis, on 6th and 7th July, and from the ash plain site (~2300 m from the plume) to the north-northwest

on 8th and 9th July (see Figure 2 for locations). The UV cameras were also operated on 11th July, however inclement weather and grounding of the plume prevented reliable data processing for that day. During the measurement days, the plume direction varied from west to northwest, with dry and predominantly cloud-free weather (bar a brief period of rain on 9th July). Of the five days on which measurements were attempted, we acquired high-quality data on four of the days, amassing 16 h of imagery across these days.

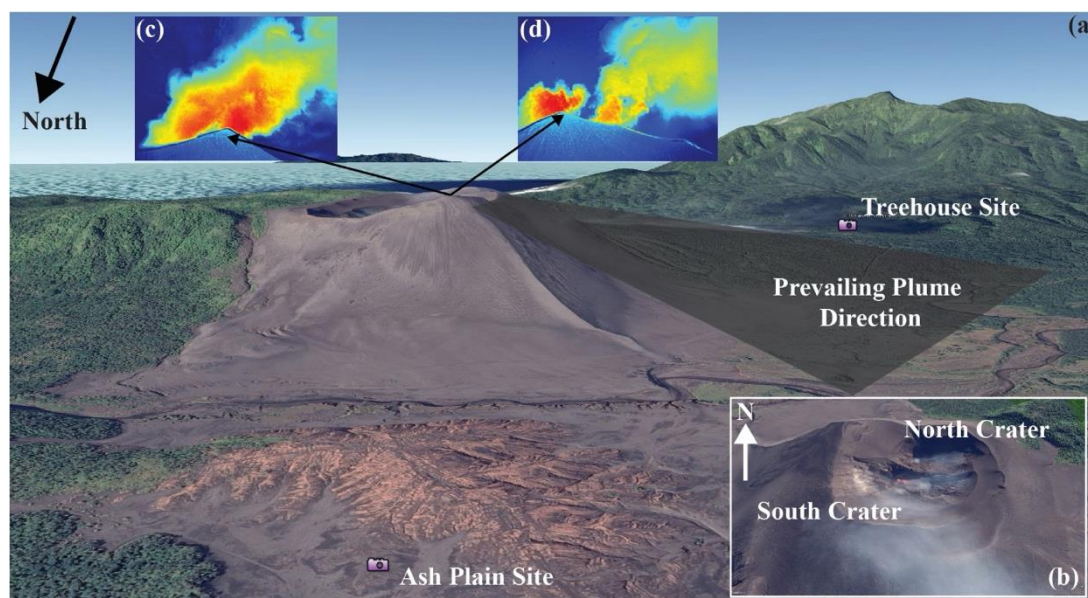


Figure 2. (a) An elevation-based perspective of the low summit of Yasur volcano, along with measurement positions and the prevailing plume transport direction, with the inset (b) showing a close-up of the summit crater. (c) A typical view of the plume, with red colours representing higher concentrations of SO₂, showing clear mixing between plumes from different vents. (d) An example of where it was possible to differentiate between emissions from both craters. Imagery is from Google Earth®.

The camera images were captured with acquisition rates of 0.5–0.25 Hz, with additional collection of clear sky images prior to the plume sequences' capture, which are required in the processing routine to account for vignetting effects. Dark images were also acquired for each sequence to enable subtraction of dark noise. We conducted frequent calibrations using gas cells with known SO₂ column densities (0, 412, and 1613 ppm m, with a manufacturer quoted error of 10%) between measurement sequences at least every 1–1.5 h, with more frequent calibration when light conditions changed more rapidly. The data were then processed following the commonly applied protocols, which have already been extensively described in the literature [39,70,74,75] (i.e., aligning images, selecting a clear sky background region and choosing a plume cross-section along which to determine integrated column amounts (ICA), before multiplying by the plume speed to calculate the flux). For the resulting flux data time series, we determined the data distribution statistically with the Kolmogorov–Smirnov normality test to inform on appropriate measures of central tendency. The data were all non-normally distributed, therefore the median was used in the further calculations, which are detailed below. However, we continued to detail both mean and median values.

A goal of this study was to attempt to differentiate degassing fluxes from each of the vents. However, it was not possible to do this rigorously and at all times, given that changes in wind shear and crater-derived eddying led to time-varying separation or overlap of individual plumes [76,77], creating difficulties in resolving emissions from the individual vents. Indeed, the plume predominantly appeared well-mixed on emergence from the summit crater (Figure 2c). However, at times, the view from the ash plain site did allow us to identify gas pulses from two distinct sources, likely corresponding

to the two craters associated with explosions, where distinct gas pulses could be spatially resolved (Figure 2d).

3.1. Particle Image Velocimetry (PIV) for Plume Velocity Determination

One of the most significant and yet frequently overlooked errors in UV camera image analysis is that associated with plume velocity determination, for which three main methods are commonly used: cross-correlation [78,79], optical-flow [71,73,80–83], and manual tracking [84]. The optimal method will largely be determined by the plume conditions, as no single method is ideally suited to all situations. Manual tracking is suitable for stable plumes travelling at slow velocities or for measurements at greater distances from the plume, where cross-correlation and optical-flow are less desirable, as the plume is more dilute and fewer pixels containing SO₂ are available for the analysis. Cross-correlation is preferred for broadly homogenous plumes that are well-mixed and undergo little turbulence (e.g., whereby eddying can cause SO₂ within parts of the plume to travel backwards relative to the bulk plume vector of motion e.g., the wind direction). Optical flow methods are well suited to high velocity plumes, where the velocity field over the plume profile is non-constant (e.g., due to pulsed gas outputs from craters, associated with Strombolian explosions or puffing) [80,82,83,85].

In this study, we encountered difficulties in using these traditional methods. Indeed, our goal was to find one method to use on all separate acquisitions to maintain consistency. In particular, efficient mechanisms for tracking pulses of gas in a large dataset were required. Indeed, cross-correlation (which tracks the delay time between two integration lines of known distances) sometimes failed, likely because of turbulent motion in the plume altering arrival times in the peaks of the gas release. Furthermore, this approach does not cope well with the transient increases in gas velocity associated with impulsive gas release during Strombolian explosions. Hence, this method is probably the least favourable in this context. A lack of plume structure (increased homogeneity and plumes that filled more of the field of view) appeared to lead to the failure of the Farneback optical flow algorithm for some of the acquisitions [65,73,80]. We, therefore, instead adopted the use of particle image velocimetry (PIV) for plume velocity determination, as this successfully allowed plume velocity analysis across all separate acquisitions, maintaining consistency. PIV was briefly discussed by Kern et al. [74]. Previous use of PIV in a volcanic context has included tracking of lava lake velocity at Masaya [77], and it is similar to the pyroclast tracking velocimetry used in [59,86]. Here, we used PIVlab, a user-friendly MATLAB toolbox and app [87,88]. PIV works by comparing image pairs in sequences and looking for differences between them through two methods: direct cross-correlation and through the correlation of Fourier transforms. Both of these methods are conducted on integration areas (here we used three) with decreasing sizes on each pass. The end result is a velocity grid for the whole plume image, similar to those grids produced during the application of optical flow [73,80] (see Figure 3a).

We found that by using PIV we were able to detect velocity differences in even the more homogenous plumes (i.e., with a quasi-uniform SO₂ distribution across most of the plume, except during Strombolian explosions). PIV was used to extract velocity components corresponding to each image pixel perpendicular to the integration line used in the ICA determination. Here, rather than using a single plume speed perpendicular to the integration line, the plume velocity vectors per pixel were multiplied by the pixel's SO₂ column amount, then these ICAs per-pixel were summed over the plume profile (see Figure 3). The PIV analyses show temporal and spatial variability in plume velocity, capturing a heterogeneity that is a real feature of the plume motion, yet which is not captured by cross-correlation or manual tracking. We report errors for the PIV analysis as the length of the integration line at given distance to the plume corresponding to each pixel divided by the lowest image capture frequency. For the ash plain site this equates to an error of $2 \pm 0.3 \text{ ms}^{-1}$ or $\sim \pm 15\%$, and for the treehouse site this equates to an error of $5 \pm 0.6 \text{ ms}^{-1}$ or $\sim \pm 9\%$. These error estimates are based on typical plume speeds for each site.

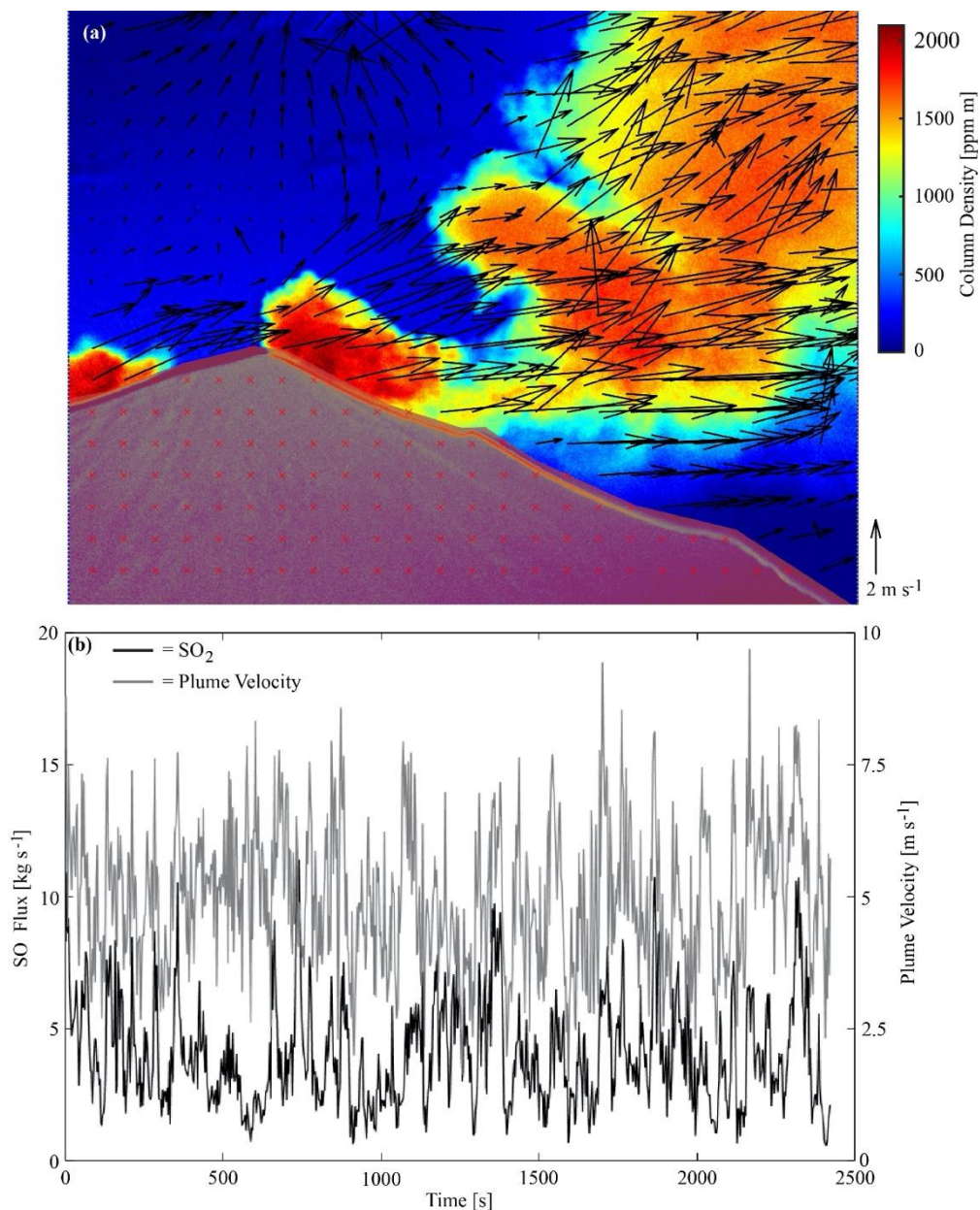


Figure 3. (a) Example plume vectors generated during PIV analysis for movement from one frame to the next, superimposed over an SO₂ absorption image. (b) Example median plume velocity across the integration line and SO₂ fluxes for a time interval of 2500 s on 7th July 2018, showing clear accelerations in plume velocities during Strombolian explosions.

3.2. Estimation of a Total UV Camera Measurement Error

Here, we highlight the range of possible error sources and perform additional analyses on our data pertaining specifically to the calibration curve drift, plume orientation, and plume distance. The final determined values for error (in Table 1) are our best possible estimates on the basis of the available information and protocols applied in-the-field, which wherever possible were designed to minimise error. The final total of the combined errors was the root-mean-square (RMS) error of all the separate sources, as detailed below.

Table 1. A summary of errors from UV camera measurements of SO₂ fluxes at Yasur volcano in July 2018, including short comments and the total root-mean-square (RMS) error. The bold emphasise different bits of data below.

	Treehouse	Ash Plain	Comments
Distance	1900 m	2300 m	–
Description	Error	Error	–
Light Dilution	+20%	+20%	Underestimation only, low given plume proximity.
Gas Cell Concentration	±10%	±10%	Manufacturer quoted
Calibration drift	±15%	±15%	Changing calibration conditions (see text)
Plume Velocity	±9	±15%	Based on pixel size (see text)
Plume Direction	±5%	±5%	Based on coincident UV camera data
Plume Distance	±18%	±18%	Based on plume deviation of 200 m
Ash content	–	–	Underestimation, not quantifiable
RMS Error	–11.2%/+13.9%	–12.2%/+14.7%	Note the higher error related to underestimation (positive error)

The effects of light dilution were quantified at a range of volcanic gas plume targets—SO₂ mass column amounts may have been underestimated by ~10–60% over a range of distances (2.1 km to 6.5 km) and conditions, from hazy through to very clear [89]. Light dilution has a larger effect during hazier conditions, which were not present during our successful measurement days. Ilanko et al. [84] calculated that at ~10.3 km distance from the plume (during clear conditions at Sabancaya volcano, Peru), SO₂ fluxes could be underestimated by 2.5 times, while at 4.25 km SO₂ fluxes could be underestimated by 1.5 times (which would correspond to ~1.18 times (18%) at our maximum distance of 2300 m at Yasur). It is important to note that light dilution estimates are very specific to the measurement location and conditions. Given our range of distances to the plume and clear measurement conditions we, therefore, suggest that the error relating to light dilution was < +20%. We also note that the plume was not optically thick, except following ash-rich Strombolian explosions. Unfortunately, exact errors due to scattering of UV by ash were currently not quantifiable, but ash within the plume would likely lead to an underestimation of SO₂ column amounts [38,90]. We attempted to minimise this error by integrating away from the summit area, where the plume was visibly less ash-rich and more transparent. We also further note that the peaks in gas flux from Strombolian explosions were well defined within the resulting dataset (Figure 3).

Gas cell calibrations change throughout the day in response to the position of the sun and changing illumination as a result of background clouds, with changes in gas cell calibrations potentially leading to over-estimation in SO₂ column densities of up to 60% [91]. Figure 4 shows the changes in the calibration slope coefficient (between regressions of the apparent absorbance coefficient and column density) throughout the day from the time of the first calibration (rather than using UTC), showing variations ranging from 1.22×10^{-4} to 1.46×10^{-4} for this parameter. When taking into account this characterised range for the slope of 2.4×10^{-5} and the broad assumption (for indicative purposes) that there is a linear change between the first point and the highest point (corresponding to maximum solar zenith angle), we arrive over 122 min between these points at a 1.97×10^{-7} increase in the slope coefficient per minute. This would equate to a potential change in error of ~0.16% per minute, which expanded over an hour could become 9.6%, or for our maximum intercalibration interval of ~95 min, an error of 15.2%. It is possible, therefore, that any underlying trends in apparent gas emission rates below these thresholds are not differentiable from this error, i.e., an increase or decrease in flux at a rate of <~0.16% per minute. We suggest, therefore, that errors from cell calibration (notwithstanding the ~±10% manufacturer-quoted cell content error) amount to a maximum of ±15% for our measurement period.

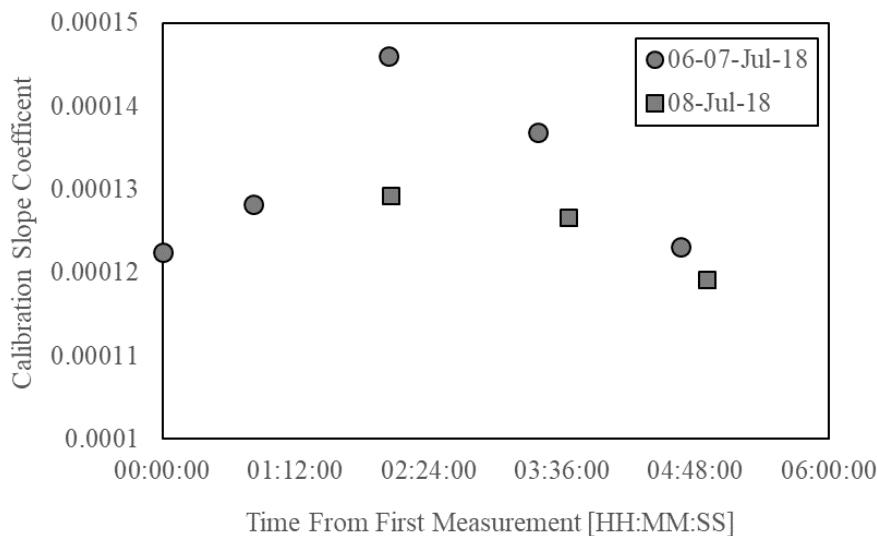


Figure 4. Example calibration slope coefficients (derived from regressions of gas cell concentrations against apparent absorbance) from two days of data. Timings are from the time of the first calibration on each of these measurement days. Note that the coefficient peaks towards solar noon.

We used fixed distances of 1900 and 2300 m from the camera to the plume for our retrieval calculations for data from the treehouse and ash plain sites, respectively. By repeating the same retrievals at different distances, for the ash plain data we determined that a 100 m error in the plume distance leads to a <5% difference in computed gas masses across the plume cross-section (with underestimation of this distance corresponding to underestimation of the gas mass) and a 200 m error in distance to <9% error. Comparisons of the same test dataset with different velocities in PIV analyses corresponding to the different distances showed variations ranging 1–7% with the 100 m error and 5–11% in the 200 m case. The combined effects of distance uncertainties on mass and velocity gave error ranges of 7–10% for fluxes at 100 m distance and 16–18% for 200 m. We, therefore, take the maximum value here of ~18% and apply this conservatively to our entire dataset.

Given the changes in plume direction, the orientation with which the integration line bisects the plume is also relevant in consideration of the measurement uncertainty [92]. To investigate this, we used overlaps between data from two synchronously acquiring cameras at the same site (Figure 5), which had slightly different plume views, and hence slightly different integration line orientations relative to the plume geometry. This simulated the time-dependent effect of the plume moving in response to changing wind conditions with respect to a fixed integrated column amount line. In this case, the two datasets were cross-correlated and shifted by the lag corresponding to the maximum correlation to account for different transport times from the source to the two cameras' different integration lines. The calculated difference in flux retrieval from the two units based on comparing the acquired median values per unit was $\sim\pm 5\%$. To calculate the RMS error, we took the RMS of all error sources, which led to a positive error (an underestimation) or a negative error (an overestimation) separately (see Table 1 for a summary). Our total estimated RMS errors were, therefore, $-11.2\%/+13.9\%$ for the treehouse site and $-12.2\%/+14.7\%$ for the ash plain site (i.e., it is more likely that our data were underestimated).

In addition, we also report on the computed flux data in Figure 6 (which documents the retrieved data from the entire campaign) during periods when the plume grounded, e.g., the integration line could not cover the entire plume cross-section, as well as episodes of heavy rainfall. During these periods, median SO_2 fluxes were underestimated significantly by ~ 4.3 – 4.4 and 5.6 – 7.3 times, respectively, based on comparisons with median values of retrieved fluxes on either side of these episodes. Whilst the data captured under these circumstances were not used in the foregoing analysis, nor considered representative of the volcanic outgassing, they are reported here to illustrate the significant error to which these effects give rise.

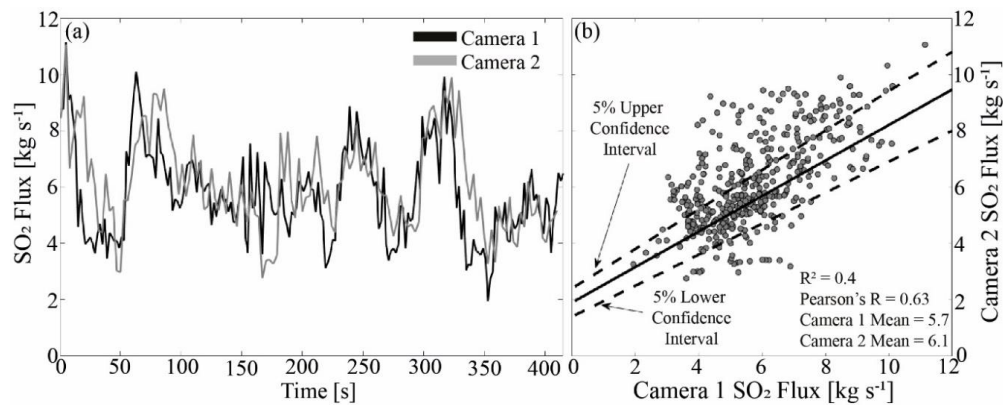


Figure 5. (a) Example period of overlapping data from two separately acquiring synchronous cameras, which viewed the plume from slightly different orientations. One dataset has been shifted by the lag value, which generated the maximum correlation coefficient, following the cross-correlation between the two series in an attempt to best temporally match the data. Note that there are differences in the magnitudes of peaks and troughs in the different data series, even when shifted relative to one another in this way, due to smoothing or turbulence during plume movement through the atmosphere and the slightly different views of the units through the plume. (b) A linear regression model ($R^2 = 0.4$) is shown, demonstrating the best fit between time series data from the two cameras, as well as confidence intervals. The statistical parameters are similar, but there are differences in peaks and troughs between the two datasets.

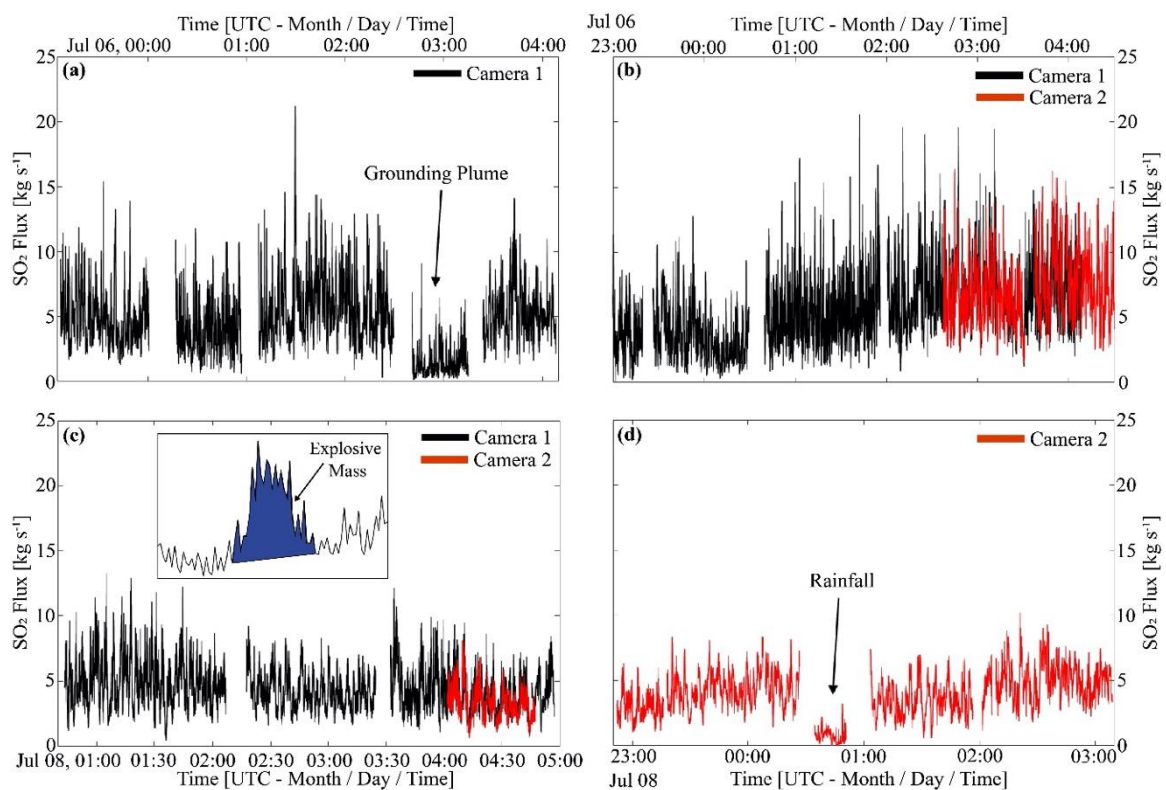


Figure 6. (a–d) Retrieved gas fluxes, where clear peaks correspond to Strombolian explosions, for all the image data captured during the observation period; also highlighted are periods where the plume was grounded (a) and heavy rainfall was encountered (d). (c) An example of the explosive mass determination, where integration occurs below the explosion peak (e.g., shaded blue area), above the background levels.

4. Results and Discussion

4.1. SO₂ Fluxes and Estimates of the Masses of Gas Emitted during Strombolian Explosions

Time series gas fluxes are shown in Figure 6, with a summary of daily statistics in Table 2. The median flux across the four days of measurements was 4.5 kg s⁻¹ and the mean was 4.9 kg s⁻¹, reflecting the peaks in SO₂ flux associated with frequent Strombolian explosions. These gas fluxes correspond to a daily median and mean of 389 and 423 t d⁻¹ across the measurement period. Daily statistics are given in Table 2. The median SO₂ fluxes ranged between 4.0 and 5.1 kg s⁻¹ across the measurement days, while the daily means ranged from 4.1 to 5.5 kg s⁻¹. The time series data are suggestive of gradual changes in background SO₂ emissions over several hours, but it is not clear whether these were real or a product of artefact error. A shift in activity is, however, plausible based on the observation of large Strombolian explosions with visible ballistics and shockwaves, particularly on 8th and 9th July, when lower fluxes were measured.

Table 2. A summary of measurement durations and SO₂ flux statistics for daily UV camera measurements at Yasur Volcano in July 2018. UTC is Coordinated Universal Time.

Date (UTC)	05–06/07/18	06–07/07/18	08/07/18	08–09/07/18
Date (Local)	06/07/18	07/07/18	08/08/18	09/08/18
Time series duration (hh:mm)	4:15	04:42	03:54	03:33
Total time (hh:mm)	05:01	05:31	04:14	04:17
Mean (kg/s)	5.2	5.5	4.5	4.1
Median (kg/s)	4.7	5.1	4.2	4.0
Standard Deviation	2.2	2.5	1.7	1.5
Coefficient of Variation	42%	45%	38%	37%

The masses of SO₂ released during each Strombolian explosion were calculated by integrating beneath the explosive pulse and summing the total SO₂ released, following Tamburello et al. [38] (see Figure 6c). However, a challenge here was that the onsets of Strombolian explosions were not visible within the imagery (i.e., vents were at depth within the crater). We used two methods to determine when explosions occurred within the UV camera imagery. Firstly, gas pulses in the camera images must be observed to originate and visibly accelerate above the rim of the summit crater (see Figure 1a) to confirm that an explosion occurred. Secondly, where gas burst traces in the flux time series were noted, showing the characteristic coda (a period of elevated flux following a Strombolian explosion, which gradually declines) detailed in Pering et al. [37] (see Figure 6c). The number of explosions was probably underestimated using these methods; however, the resulting estimation of the SO₂ released during each explosion was useful for comparison with literature values (Table 3). Overall, the SO₂ masses released were estimated for 135 explosions across five days. The mean masses of SO₂ released increased from 6th to 9th July 2018, which is consistent with visual observations of more powerful explosions on 8th and 9th July 2018.

The range of SO₂ masses released during Strombolian explosions at Yasur of 8–81 kg (mean 32 kg) is similar to the range estimated by Tamburello et al. [38] at Stromboli, who found a range of 2–55 kg (mean of 20 kg). However, these values are higher than those observed at Etna during mild Strombolian activity [15], which ranged from 0.1 to 14 kg. Gas ratios (SO₂, H₂S, H₂O, and CO₂) derived from a combined Fourier transform infrared spectroscopy (FTIR) and MultiGAS study from 6th to 16th July 2018 showed distinct gas compositions during passive and explosive activity [29]. Gases emitted during Strombolian activity had molar ratios of: CO₂/SO₂ = 2.85 ± 0.17; H₂O/SO₂ = 315 ± 71.8; SO₂/HCl = 1.7 ± 0.22. Using these data, we can estimate total gas slug masses, as shown in Table 3. The mean total gas mass emitted during Strombolian explosions at Yasur was 2960 kg, with a range of 910–5940 kg. These estimates are similar to the range of 170–1674 kg for Strombolian

explosions at Pacaya [6], whereas at Stromboli the explosion masses ranged from 44 to 238 kg according to Barnie et al. [93] and from 2 to 1425 kg as determined by Delle Donne et al. [34].

Table 3. A breakdown of daily SO₂ explosion mass data. Also displayed are percentages indicating the partitioning of gas masses between passive and explosive degassing. Below this the total gas slug masses are shown, where lower and upper ratios refer to the ranges indicated in determined active molar ratios by Woitischek et al. (Table 3; CO₂/SO₂ = 2.85 ± 0.17; H₂O/SO₂ = 315 ± 71.8; SO₂/HCl = 1.6 ± 0.22).

Date (UTC)	05/07/2018	06/07/2018	07/07/2018	08/07/2018	09/07/2019	Total
Explosions Counted	8	43	39	36	9	135
						Mean (Error)
SO ₂ Min (kg)	10.2	8.9	8	12	10	9.8 (±1.4)
SO ₂ Mean (kg)	26.9	22.1	27	39	45	32.0 (±4.7)
SO ₂ Max (kg)	64.1	44.9	62	81	69	64.2 (±9.4)
Passive ¹ %	66	64	70	78	68	69
Explosive ¹ %	34	36	30	22	32	31
Total Slug Masses from Lower Ratios						
Min (kg)	712	625	575	822	721	691
Mean (kg)	1884	1550	1892	2713	3164	2241
Max (kg)	3020	3148	4370	5678	4813	4206
Total Slug Masses from Mean Ratios						
Min (kg)	940	824	759	1084	952	912
Mean (kg)	2486	2046	2497	3579	4175	2957
Max (kg)	5929	4153	5767	7493	6350	5938
Total Slug Masses from Upper Ratios						
Min (kg)	1167	1024	942	1347	1182	1132
Mean (kg)	3088	2541	3102	4446	5186	3673
Max (kg)	7365	5159	7163	9307	7888	7376

¹ These values are from the statistical calculation of this paper (Section 4.2).

4.2. Simple Statistical Separation of Passive and Explosive Degassing

Others have studied the ratios of explosive-to-passive release during Strombolian explosions on Stromboli [38] and Etna [15]. Here, we attempt to expand on this by using a simple statistical measure involving the moving minimum (which traces the lower values in a dataset over a defined window, similarly to the moving mean) to estimate the passive release of gas through time, which when subtracted from total flux provides an approximate estimate of passive vs. explosive release. This was necessary, as our manual selection of events missed or excluded several Strombolian explosions. Our approach is similar to the automated method of Delle Donne et al. [82], which involved finding local peaks in time series data. For an example period (Figure 7), we highlight the moving minimum, which is set to a window size of 20 s, which is generally the characteristic timeframe of large peaks and troughs associated with Strombolian explosions [37,82]. Note that using this moving minimum method, an oscillation (non-uniform) background is apparent. Delle Donne et al. [82] also showed a fluctuation in the passive background between Strombolian explosions. This background is used as a best estimate solely to extract the explosive contribution. In this instance at Yasur, a moving minimum over a 20 s window proved best, given the higher frequency of explosive events; however, with a greater timeframe between events, the moving median may be a better measure. We also prefer this statistical estimation technique over using our estimated SO₂ masses, given that the latter required manual selection of Strombolian explosions. This simple moving minimum approach could be readily and simply automated for routine monitoring of activity from Strombolian-explosion-producing volcanic systems.

Daily estimates of the passive and active degassing contributions are shown in Table 3, with a mean of 69% passive release compared to 31% explosive release. These estimates are similar to those estimated at Stromboli, showing 77% passive release compared to 23% explosive release (termed “active”, which also includes puffing); and at Etna, showing 67% passive release compared to 33%

explosive release [15]. These datasets serve to illustrate the dominance of passive degassing in the gas emission budget at volcanoes that exhibit Strombolian activity. On the 8th July 2018, we calculated a higher passive degassing contribution of 78%. This day was characterised by higher SO_2 masses emitted during individual explosions but lower overall SO_2 fluxes. These features may be consistent with a degassing magma column beneath a thicker, more viscous, impermeable crystal-rich plug, requiring a higher gas mass to drive more powerful explosions [29,55,94], which is consistent with visual observations.

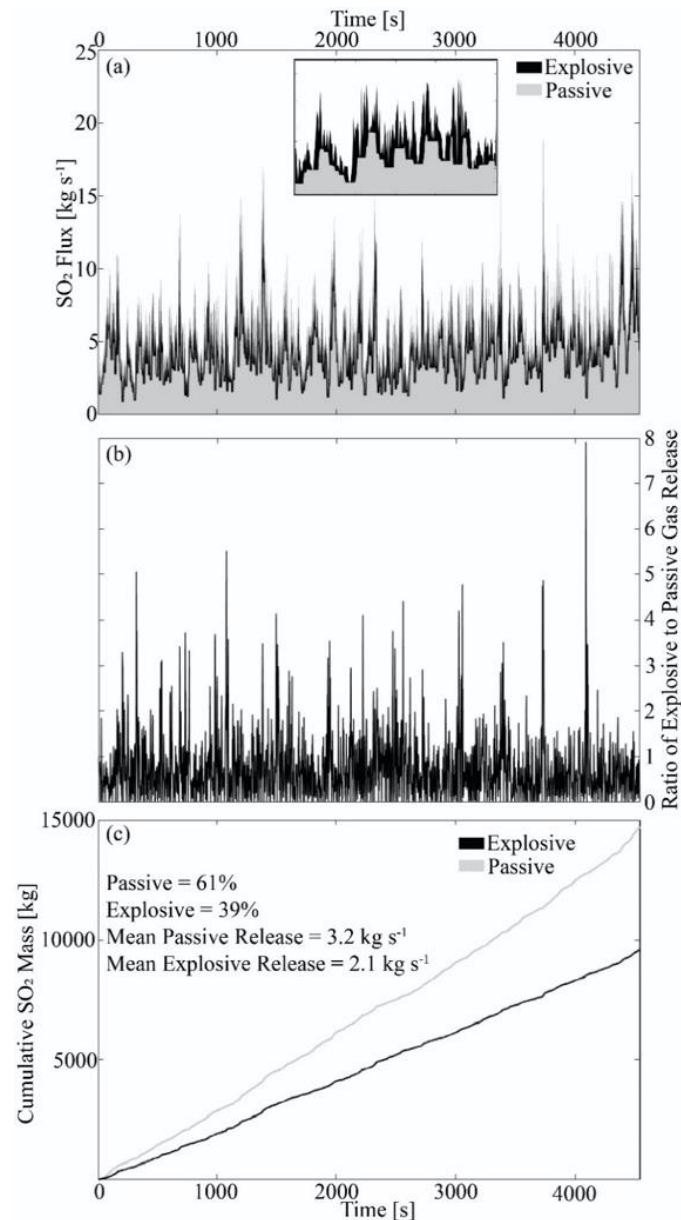


Figure 7. (a) Separation of passive and explosion gas release for a period on the 7th July with (inset) an enhanced illustration of the simple statistical moving-minimum-based model, showing oscillation in the passive background degassing overtopped by explosive contributions. (b) The ratio of passive-to-explosive degassing and (c) a cumulative plot showing the division between passive and explosive gas release. Here, passive and explosive releases have been cumulatively summed to show the change through time at the sampling frequency. The passive-to-explosive ratio is the ratio of the final sum of the gas release.

4.3. Models of Gas Slug Behaviour

Using our determined values for total slug mass, we can estimate slug lengths using the static pressure model of Del Bello et al. [24]. We use fixed values of 2600 kg m^{-3} and 1000 Pa s for density and viscosity, respectively, with an atmospheric pressure of $101,325 \text{ Pa}$. The only parameter we vary in the model is that of the conduit diameter, which we step up from 3 to 7 m. We use only the mean explosive gas ratios and masses (and not the range obtained when including error) for simplicity. It should be noted that the molar $\text{H}_2\text{O}/\text{SO}_2$ ratio is high and variable [29]. As water is the gas that contributes most to the mass of the slug, it is likely that our determined total gas masses are an overestimation. Our results are summarised in Table 4. We determine slug lengths ranging 188–609 m (median and mean of 347 and 366 m, respectively) for a conduit diameter of 3 m. However, this reduces to 76–260 m (median and mean of 146 and 154 m, respectively) for a conduit diameter of 7 m. Kremers et al. [12] calculated lower values of 59–244 m using seismoacoustic data. It would, therefore, seem that a larger conduit diameter may be more plausible at Yasur, which may bifurcate or split at very shallow depths [55].

Table 4. A summary of gas slug volumes and lengths using the model of Del Bello et al. (2012) and based on gas flux and composition data acquired during Strombolian activity at Yasur volcano in July 2018.

Statistic	Slug Volume (m^3)	D = 3 m	D = 4 m	D = 5 m	D = 6 m	D = 7 m
Minimum (m)	4286	188	139	110	90	76
Median (m)	14055	347	259	205	170	146
Mean (m)	15556	366	272	217	180	154
Maximum (m)	42337	609	455	364	303	260

D is the conduit diameter.

5. Summary and Conclusions

In this work, we highlighted the utility of using low-cost solar-powered Raspberry Pi UV cameras for prolonged field campaigns. We continuously imaged the volcanic plume to yield both the velocity using a PIV method [87,88] and SO_2 fluxes over periods of several hours per day, at temporal resolutions of up to 0.5 Hz, with brief pauses for calibration. SO_2 fluxes were determined, with daily means of $4.1\text{--}5.5 \text{ kg s}^{-1}$ (medians from $4.0\text{--}5.1 \text{ kg s}^{-1}$), which are within the ranges of those measured previously at Yasur using ground-based methods, with values of 2.5 to 17.2 kg s^{-1} [13,62]. SO_2 masses emitted during individual Strombolian explosions ranged from 8 to 81 kg, similarly to events at Stromboli, which were associated with emission values ranging $2\text{--}55 \text{ kg SO}_2$ [38]. By using a simple statistical measure, we estimate that passive degassing at 69% is the dominant mode of degassing at Yasur, compared to 31% explosive serve. Our observations suggest that periods of lower gas output are associated with conduit sealing and more violent explosions, however a longer dataset would be needed to test this hypothesis substantively. By combining SO_2 explosion masses with gas ratios [29], we determined total mean explosion gas masses of $910\text{--}5940 \text{ kg}$, which using the model of [24] correspond to slug lengths of $76\text{--}260 \text{ m}$ if a larger conduit diameter of 7 m is used. Smaller conduit diameters lead to longer slug lengths of $\sim 188\text{--}600 \text{ m}$ at 3 m diameter, larger than those estimated previously at $\sim 59\text{--}244 \text{ m}$ [12]. The data presented here represent an important addition to our gas-data-based characterisation of the spectrum of Strombolian activity across the globe.

Author Contributions: Conceptualization, T.D.P.; Data curation, A.A.; Formal analysis, T.I. and R.D.; Investigation, T.I., J.W. and E.G.; Methodology, T.I., T.D.P., T.C.W., R.D., A.J.S.M. and M.E.; Resources, A.A.; Software, T.C.W.; Writing—original draft, T.D.P.; Writing—review & editing, T.D.P., A.A., A.J.S.M. and M.E. All authors have read and agreed to the published version of the manuscript.

Funding: J.W. and M.E. were supported by the Natural Environment Research Council (grant number NE/L002507/1); by the postgraduate travel funds received from Fitzwilliam College; by the Elspeth Matthews grant given by the Royal Geological Society; by the Mary Euphrasia Mosley, Sir Bartle Frere, and Worts travel fund report given by the University of Cambridge; and by the Exzellenzstipendium received by WKO. A.A. acknowledges

funding support from the Alfred P. Sloan Foundation via the Deep Carbon Observatory (UniPa-CiW subcontract 10881-1262) and from MIUR (under grant n. PRIN2017-2017LMNLAW). T.D.P. acknowledges the support of the Royal Society (RG170226). T.I. is a Commonwealth Rutherford Fellow, funded by the UK government. A.McG. acknowledges support from the Rolex Institute.

Acknowledgments: We would like to thank the Vanuatu Meteorology and Geohazards Department for permission to conduct this fieldwork, Kelson and Joyce Hosea for their hospitality at the Jungle Oasis, and Roger for his assistance in the field

Conflicts of Interest: The authors declare no conflict of interest.

References

1. Wilkes, T.; McGonigle, A.; Pering, T.; Taggart, A.; White, B.; Bryant, R.; Willmott, J.; Wilkes, T.C.; McGonigle, A.J.S.; Pering, T.D.; et al. Ultraviolet Imaging with Low Cost Smartphone Sensors: Development and Application of a Raspberry Pi-Based UV Camera. *Sensors* **2016**, *16*, 1649. [[CrossRef](#)] [[PubMed](#)]
2. Wilkes, T.; Pering, T.; McGonigle, A.; Tamburello, G.; Willmott, J.; Wilkes, T.C.; Pering, T.D.; McGonigle, A.J.S.; Tamburello, G.; Willmott, J.R. A Low-Cost Smartphone Sensor-Based UV Camera for Volcanic SO₂ Emission Measurements. *Remote Sens.* **2017**, *9*, 27. [[CrossRef](#)]
3. Blackburn, E.A.; Wilson, L.; Sparks, R.S.J. Mechanisms and dynamics of strombolian activity. *J. Geol. Soc. Lond.* **1976**, *132*, 429–440. [[CrossRef](#)]
4. Taddeucci, J.; Edmonds, M.; Houghton, B.; James, M.R.; Vergnolle, S. Hawaiian and Strombolian Eruptions. In *The Encyclopedia of Volcanoes*; Elsevier: Amsterdam, The Netherlands, 2015; pp. 485–503.
5. Pering, T.D.; McGonigle, A.J.S. Combining Spherical-Cap and Taylor Bubble Fluid Dynamics with Plume Measurements to Characterize Basaltic Degassing. *Geosciences* **2018**, *8*, 42. [[CrossRef](#)]
6. Patrick, M.R.; Harris, A.J.L.; Ripepe, M.; Dehn, J.; Rothery, D.A.; Calvari, S. Strombolian explosive styles and source conditions: Insights from thermal (FLIR) video. *Bull. Volcanol.* **2007**, *69*, 769–784. [[CrossRef](#)]
7. Ripepe, M.; Harris, A.J.L.; Carniel, R. Thermal, seismic and infrasonic evidences of variable degassing rates at Stromboli volcano. *J. Volcanol. Geotherm. Res.* **2002**, *118*, 285–297. [[CrossRef](#)]
8. Dalton, M.P.; Waite, G.P.; Watson, I.M.; Nadeau, P.A. Multiparameter quantification of gas release during weak Strombolian eruptions at Pacaya Volcano, Guatemala. *Geophys. Res. Lett.* **2010**, *37*, L09303. [[CrossRef](#)]
9. Battaglia, A.; Bitetto, M.; Aiuppa, A.; Rizzo, A.L.; Chigna, G.; Watson, I.M.; D'Aleo, R.; Juárez Cacao, F.J.; de Moor, M.J. The Magmatic Gas Signature of Pacaya Volcano, With Implications for the Volcanic CO₂ Flux From Guatemala. *Geochem. Geophys. Geosyst.* **2018**, *19*, 667–692. [[CrossRef](#)]
10. Johnson, J.B.; Aster, R.C. Relative partitioning of acoustic and seismic energy during Strombolian eruptions. *J. Volcanol. Geotherm. Res.* **2005**, *148*, 334–354. [[CrossRef](#)]
11. Oppenheimer, C.; Lomakina, A.S.; Kyle, P.R.; Kingsbury, N.G.; Boichu, M. Pulsatory magma supply to a phonolite lava lake. *Earth Planet. Sci. Lett.* **2009**, *284*, 392–398. [[CrossRef](#)]
12. Sweeney, D.; Kyle, P.R.; Oppenheimer, C. Sulfur dioxide emissions and degassing behavior of Erebus volcano, Antarctica. *J. Volcanol. Geotherm. Res.* **2008**, *177*, 725–733. [[CrossRef](#)]
13. Ilanko, T.; Oppenheimer, C.; Burgisser, A.; Kyle, P. Transient degassing events at the lava lake of Erebus volcano, Antarctica: Chemistry and mechanisms. *GeoRes. J.* **2015**, *7*, 43–58. [[CrossRef](#)]
14. Kremers, S.; Wassermann, J.; Meier, K.; Pelties, C.; van Driel, M.; Vasseur, J.; Hort, M. Inverting the source mechanism of Strombolian explosions at Mt. Yasur, Vanuatu, using a multi-parameter dataset. *J. Volcanol. Geotherm. Res.* **2013**, *262*, 104–122. [[CrossRef](#)]
15. Bani, P.; Lardy, M. Sulphur dioxide emission rates from Yasur volcano, Vanuatu archipelago. *Geophys. Res. Lett.* **2007**, *34*, L20309. [[CrossRef](#)]
16. Oppenheimer, C.; Bani, P.; Calkins, J.A.; Burton, M.R.; Sawyer, G.M. Rapid FTIR sensing of volcanic gases released by Strombolian explosions at Yasur volcano, Vanuatu. *Appl. Phys. B* **2006**, *85*, 453–460. [[CrossRef](#)]
17. Pering, T.D.; Tamburello, G.; McGonigle, A.J.S.; Aiuppa, A.; James, M.R.; Lane, S.J.; Sciotto, M.; Cannata, A.; Patanè, D. Dynamics of mild strombolian activity on Mt. Etna. *J. Volcanol. Geotherm. Res.* **2015**, *300*, 103–111. [[CrossRef](#)]
18. Aiuppa, A.; Coco, E.L.; Liuzzo, M.; Giudice, G. Terminal Strombolian activity at Etna's central craters during summer 2012: The most CO₂-rich volcanic gas ever recorded at Mount Etna. *Geochem. J.* **2016**, *50*, 123–138. [[CrossRef](#)]

19. Branca, S.; del Carlo, P. Types of eruptions of Etna volcano AD 1670–2003: Implications for short-term eruptive behaviour. *Bull. Volcanol.* **2005**, *67*, 732–742. [[CrossRef](#)]
20. Shinohara, H.; Witter, J.B. Volcanic gases emitted during mild Strombolian activity of Villarrica volcano, Chile. *Geophys. Res. Lett.* **2005**, *32*, L20308. [[CrossRef](#)]
21. Garcés, M.A.; Hagerty, M.T.; Schwartz, S.Y. Magma acoustics and time-varying melt properties at Arenal Volcano, Costa Rica. *Geophys. Res. Lett.* **1998**, *25*, 2293–2296. [[CrossRef](#)]
22. Szramek, L.; Gardner, J.E.; Larsen, J. Degassing and microlite crystallization of basaltic andesite magma erupting at Arenal Volcano, Costa Rica. *J. Volcanol. Geotherm. Res.* **2006**, *157*, 182–201. [[CrossRef](#)]
23. Gaudin, D.; Taddeucci, J.; Scarlato, P.; del Bello, E.; Ricci, T.; Orr, T.; Houghton, B.; Harris, A.; Rao, S.; Bucci, A. Integrating puffing and explosions in a general scheme for Strombolian-style activity. *J. Geophys. Res. Solid Earth* **2017**, *122*, 1860–1875. [[CrossRef](#)]
24. Laiolo, M.; Massimetti, F.; Cigolini, C.; Ripepe, M.; Coppola, D. Long-term eruptive trends from space-based thermal and SO₂ emissions: A comparative analysis of Stromboli, Batu Tara and Tinakula volcanoes. *Bull. Volcanol.* **2018**, *80*, 1–19. [[CrossRef](#)]
25. Vergnolle, S.; Boichu, M.; Caplan-Auerbach, J. Acoustic measurements of the 1999 basaltic eruption of Shishaldin volcano, Alaska 1. Origin of Strombolian activity. *J. Volcanol. Geotherm. Res.* **2004**, *137*, 109–134. [[CrossRef](#)]
26. Del Bello, E.; Llewellyn, E.W.; Taddeucci, J.; Scarlato, P.; Lane, S.J. An analytical model for gas overpressure in slug-driven explosions: Insights into Strombolian volcanic eruptions. *J. Geophys. Res. Solid Earth* **2012**, *117*, B02206. [[CrossRef](#)]
27. Seyfried, R.; Freundt, A. Experiments on conduit flow and eruption behavior of basaltic volcanic eruptions. *J. Geophys. Res.* **2000**, *105*, 23727. [[CrossRef](#)]
28. James, M.R.; Lane, S.J.; Corder, S.B. Modelling the rapid near-surface expansion of gas slugs in low-viscosity magmas. *Geol. Soc. Lond. Spec. Publ.* **2008**, *307*, 147–167. [[CrossRef](#)]
29. Barth, A.; Edmonds, M.; Woods, A. Valve-like dynamics of gas flow through a packed crystal mush and cyclic strombolian explosions. *Sci. Rep.* **2019**, *9*, 821. [[CrossRef](#)]
30. Suckale, J.; Keller, T.; Cashman, K.V.; Persson, P.O. Flow-to-fracture transition in a volcanic mush plug may govern normal eruptions at Stromboli. *Geophys. Res. Lett.* **2016**, *43*, 12071–12081. [[CrossRef](#)]
31. Woitischek, J.; Woods, A.W.; Edmonds, M.; Oppenheimer, C.; Aiuppa, A.; Pering, T.D.; Ilanko, T.; D’Aleo, R.; Garaebiti, E. Strombolian eruptions and dynamics of magma degassing at Yasur Volcano (Vanuatu). *J. Volcanol. Geotherm. Res.* **2020**, *398*, 106869. [[CrossRef](#)]
32. Pering, T.D.; Liu, E.J.; Wood, K.; Wilkes, T.C.; Aiuppa, A.; Tamburello, G.; Bitetto, M.; Richardson, T.; McGonigle, A.J.S. Combined ground and aerial measurements resolve vent-specific gas fluxes from a multi-vent volcano. *Nat. Commun.* **2020**, *11*, 3039. [[CrossRef](#)] [[PubMed](#)]
33. Pering, T.D.; McGonigle, A.J.S.; James, M.R.; Capponi, A.; Lane, S.J.; Tamburello, G.; Aiuppa, A. The dynamics of slug trains in volcanic conduits: Evidence for expansion driven slug coalescence. *J. Volcanol. Geotherm. Res.* **2017**, *348*, 26–35. [[CrossRef](#)]
34. Chouet, B.; Dawson, P.; Ohminato, T.; Martini, M.; Saccorotti, G.; Giudicepietro, F.; de Luca, G.; Milana, G.; Scarpa, R. Source mechanisms of explosions at Stromboli Volcano, Italy, determined from moment-tensor inversions of very-long-period data. *J. Geophys. Res. Solid Earth* **2003**, *108*, 2019. [[CrossRef](#)]
35. Marchetti, E.; Ripepe, M.; Harris, A.J.L.; Delle Donne, D. Tracing the differences between Vulcanian and Strombolian explosions using infrasonic and thermal radiation energy. *Earth Planet. Sci. Lett.* **2009**, *279*, 273–281. [[CrossRef](#)]
36. Delle Donne, D.; Ripepe, M.; Lacanna, G.; Tamburello, G.; Bitetto, M.; Aiuppa, A. Gas mass derived by infrasound and UV cameras: Implications for mass flow rate. *J. Volcanol. Geotherm. Res.* **2016**, *325*, 169–178. [[CrossRef](#)]
37. Johnson, J.B.; Ripepe, M. Volcano infrasound: A review. *J. Volcanol. Geotherm. Res.* **2011**, *206*, 61–69. [[CrossRef](#)]
38. McGonigle, A.J.S.; Aiuppa, A.; Ripepe, M.; Kantzas, E.P.; Tamburello, G. Spectroscopic capture of 1 Hz volcanic SO₂ fluxes and integration with volcano geophysical data. *Geophys. Res. Lett.* **2009**, *36*, 1–5. [[CrossRef](#)]

39. Pering, T.D.; McGonigle, A.J.S.; James, M.R.; Tamburello, G.; Aiuppa, A.; Delle Donne, D.; Ripepe, M. Conduit dynamics and post explosion degassing on Stromboli: A combined UV camera and numerical modeling treatment. *Geophys. Res. Lett.* **2016**, *43*, 5009–5016. [[CrossRef](#)]
40. Tamburello, G.; Aiuppa, A.; Kantzas, E.P.; McGonigle, A.J.S.; Ripepe, M. Passive vs. active degassing modes at an open-vent volcano (Stromboli, Italy). *Earth Planet. Sci. Lett.* **2012**, *359–360*, 106–116. [[CrossRef](#)]
41. McGonigle, A.J.S.; Pering, T.D.; Wilkes, T.C.; Tamburello, G.; D'Aleo, R.; Bitetto, M.; Aiuppa, A.; Willmott, J.R. Ultraviolet Imaging of Volcanic Plumes: A New Paradigm in Volcanology. *Geosciences* **2017**, *7*, 68. [[CrossRef](#)]
42. Pering, T.D.; Ilanko, T.; Liu, E.J. Periodicity in Volcanic Gas Plumes: A Review and Analysis. *Geosciences* **2019**, *9*, 394. [[CrossRef](#)]
43. Shinohara, H.; Ohminato, T.; Takeo, M.; Tsuji, H. Monitoring of volcanic gas composition at Asama volcano, Japan, during 2004–2014. *J. Volcanol.* **2015**, *303*, 199–208. [[CrossRef](#)]
44. Aiuppa, A.; Federico, C.; Giudice, G.; Gurrieri, S. Chemical mapping of a fumarolic field: La Fossa Crater, Vulcano Island (Aeolian Islands, Italy). *Geophys. Res. Lett.* **2005**, *32*, L13309. [[CrossRef](#)]
45. Pering, T.D.; Tamburello, G.; McGonigle, A.J.S.; Aiuppa, A.; Cannata, A.; Giudice, G.; Patanè, D. High time resolution fluctuations in volcanic carbon dioxide degassing from Mount Etna. *J. Volcanol. Geotherm. Res.* **2014**, *270*, 115–121. [[CrossRef](#)]
46. Jaupart, C.; Vergnolle, S. Laboratory models of Hawaiian and Strombolian eruptions. *Nature* **1988**, *331*, 58–60. [[CrossRef](#)]
47. Jaupart, C.; Vergnolle, S. The generation and collapse of a foam layer at the roof of a basaltic magma chamber. *J. Fluid Mech.* **1989**, *203*, 347–380. [[CrossRef](#)]
48. Parfitt, E.A. A discussion of the mechanisms of explosive basaltic eruptions. *J. Volcanol. Geotherm. Res.* **2004**, *134*, 77–107. [[CrossRef](#)]
49. Vergnolle, S.; Jaupart, C. Separated two-phase flow and basaltic eruptions. *J. Geophys. Res. Solid Earth* **1986**, *91*, 12842–12860. [[CrossRef](#)]
50. Gaudin, D.; Taddeucci, J.; Scarlato, P.; Harris, A.; Bombrun, M.; del Bello, E.; Ricci, T. Characteristics of puffing activity revealed by ground-based, thermal infrared imaging: The example of Stromboli Volcano (Italy). *Bull. Volcanol.* **2017**, *79*, 24. [[CrossRef](#)]
51. Carn, S.A.; Fioletov, V.E.; Mclinden, C.A.; Li, C.; Krotkov, N.A. A decade of global volcanic SO₂ emissions measured from space. *Sci. Rep.* **2017**, *7*, 1–12. [[CrossRef](#)]
52. Mori, T.; Burton, M. Quantification of the gas mass emitted during single explosions on Stromboli with the SO₂ imaging camera. *J. Volcanol. Geotherm. Res.* **2009**, *188*, 395–400. [[CrossRef](#)]
53. Burton, M.; Allard, P.; Mure, F.; La Spina, A. Magmatic Gas Composition Reveals the Source Depth of Slug-Driven Strombolian Explosive Activity. *Science* **2007**, *317*, 227–230. [[CrossRef](#)]
54. James, M.R.; Lane, S.J.; Wilson, L.; Corder, S.B. Degassing at low magma-viscosity volcanoes: Quantifying the transition between passive bubble-burst and Strombolian eruption. *J. Volcanol. Geotherm. Res.* **2009**, *180*, 81–88. [[CrossRef](#)]
55. Firth, C.W.; Handley, H.K.; Cronin, S.J.; Turner, S.P. The eruptive history and chemical stratigraphy of a post-caldera, steady-state volcano: Yasur, Vanuatu. *Bull. Volcanol.* **2014**, *76*, 1–23. [[CrossRef](#)]
56. Salvatore, V.; Silleni, A.; Corneli, D.; Taddeucci, J.; Palladino, D.M.; Sottili, G.; Bernini, D.; Andronico, D.; Cristaldi, A. Parameterizing multi-vent activity at Stromboli Volcano (Aeolian Islands, Italy). *Bull. Volcanol.* **2018**, *80*, 64. [[CrossRef](#)]
57. Simons, B.C.; Jolly, A.D.; Eccles, J.D.; Cronin, S.J. Spatiotemporal Relationships between Two Closely-spaced Strombolian-style Vents, Yasur, Vanuatu. *Geophys. Res. Lett.* **2020**, *47*, e85687. [[CrossRef](#)]
58. Spina, L.; Taddeucci, J.; Cannata, A.; Gresta, S.; Lodato, L.; Privitera, E.; Scarlato, P.; Gaeta, M.; Gaudin, D.; Palladino, D.M. Explosive volcanic activity at Mt. Yasur: A characterization of the acoustic events (9–12th July 2011). *J. Volcanol. Geotherm. Res.* **2016**, *322*, 175–183. [[CrossRef](#)]
59. Meier, K.; Hort, M.; Wassermann, J.; Garaebiti, E. Strombolian surface activity regimes at Yasur volcano, Vanuatu, as observed by Doppler radar, infrared camera and infrasound. *J. Volcanol. Geotherm. Res.* **2016**, *322*, 184–195. [[CrossRef](#)]
60. Taddeucci, J.; Scarlato, P.; Capponi, A.; del Bello, E.; Cimarelli, C.; Palladino, D.M.; Kueppers, U. High-speed imaging of Strombolian explosions: The ejection velocity of pyroclasts. *Geophys. Res. Lett.* **2012**, *39*, 1–6. [[CrossRef](#)]

61. Gaudin, D.; Taddeucci, J.; Scarlato, P.; Moroni, M.; Freda, C.; Gaeta, M.; Palladino, D.M. Pyroclast Tracking Velocimetry illuminates bomb ejection and explosion dynamics at Stromboli (Italy) and Yasur (Vanuatu) volcanoes. *J. Geophys. Res. Solid Earth* **2014**, *119*, 5384–5397. [[CrossRef](#)]
62. Ripepe, M.; Harris, A.J.L.; Marchetti, E. Coupled thermal oscillations in explosive activity at different craters of Stromboli volcano. *Geophys. Res. Lett.* **2005**, *32*, 1–4. [[CrossRef](#)]
63. Ripepe, M.; Marchetti, E. Array tracking of infrasonic sources at Stromboli volcano. *Geophys. Res. Lett.* **2002**, *29*, 33.1–33.4. [[CrossRef](#)]
64. Bani, P.; Oppenheimer, C.; Allard, P.; Shinohara, H.; Tsanev, V.; Carn, S.; Lardy, M.; Garaebiti, E. First estimate of volcanic SO₂ budget for Vanuatu island arc. *J. Volcanol. Geotherm. Res.* **2012**, *211–212*, 36–46. [[CrossRef](#)]
65. Métrich, N.; Allard, P.; Aiuppa, A.; Bani, P.; Bertagnini, A.; Shinohara, H.; Parello, F.; Di Muro, A.; Garaebiti, E.; Belhadj, O.; et al. Magma and Volatile Supply to Post-collapse Volcanism and Block Resurgence in Siwi Caldera (Tanna Island, Vanuatu Arc). *J. Pet.* **2011**, *52*, 1077–1105. [[CrossRef](#)]
66. Delle Donne, D.; Ripepe, M. High-frame rate thermal imagery of strombolian explosions: Implications for explosive and infrasonic source dynamics. *J. Geophys. Res. Solid Earth* **2012**, *117*, 1–12. [[CrossRef](#)]
67. Salvatore, V.; Cigala, V.; Taddeucci, J.; Arciniega-Ceballos, A.; Peña Fernández, J.J.; Alatorre-Ibargüengoitia, M.A.; Gaudin, D.; Palladino, D.M.; Kueppers, U.; Scarlato, P. Gas-Pyroclast Motions in Volcanic Conduits During Strombolian Eruptions, in Light of Shock Tube Experiments. *J. Geophys. Res. Solid Earth* **2020**, *125*, e19182. [[CrossRef](#)]
68. Dibble, R.R.; Kyle, P.R.; Rowe, C.A. Video and seismic observations of Strombolian eruptions at Erebus volcano, Antarctica. *J. Volcanol. Geotherm. Res.* **2008**, *177*, 619–634. [[CrossRef](#)]
69. Mori, T.; Burton, M. The SO₂ camera: A simple, fast and cheap method for ground-based imaging of SO₂ in volcanic plumes. *Geophys. Res. Lett.* **2006**, *33*, L24804. [[CrossRef](#)]
70. Kantzas, E.P.; McGonigle, A.J.S.; Tamburello, G.; Aiuppa, A.; Bryant, R.G. Protocols for UV camera volcanic SO₂ measurements. *J. Volcanol. Geotherm. Res.* **2010**, *194*, 55–60. [[CrossRef](#)]
71. Kern, C.; Lübcke, P.; Bobrowski, N.; Campion, R.; Mori, T.; Smekens, J.-F.; Stebel, K.; Tamburello, G.; Burton, M.; Platt, U.; et al. Intercomparison of SO₂ camera systems for imaging volcanic gas plumes. *J. Volcanol. Geotherm. Res.* **2015**, *300*, 22–36. [[CrossRef](#)]
72. Platt, U.; Lübcke, P.; Kuhn, J.; Bobrowski, N.; Prata, F.; Burton, M.; Kern, C. Quantitative imaging of volcanic plumes—Results, needs, and future trends. *J. Volcanol. Geotherm. Res.* **2015**, *300*, 7–21. [[CrossRef](#)]
73. Gliß, J.; Stebel, K.; Kylling, A.; Dinger, A.; Sihler, H.; Sudbø, A. Pyplis—A Python Software Toolbox for the Analysis of SO₂ Camera Images for Emission Rate Retrievals from Point Sources. *Geosciences* **2017**, *7*, 134. [[CrossRef](#)]
74. Kern, C.; Sutton, J.; Elias, T.; Lee, L.; Kamibayashi, K.; Antolik, L.; Werner, C. An automated SO₂ camera system for continuous, real-time monitoring of gas emissions from Kīlauea Volcano’s summit Overlook Crater. *J. Volcanol. Geotherm. Res.* **2014**, *300*, 81–94. [[CrossRef](#)]
75. D’Aleo, R.; Bitetto, M.; Delle Donne, D.; Tamburello, G.; Battaglia, A.; Coltelli, M.; Patanè, D.; Prestifilippo, M.; Sciotto, M.; Aiuppa, A. Spatially resolved SO₂ flux emissions from Mt Etna. *Geophys. Res. Lett.* **2016**, *43*, 7511–7519. [[CrossRef](#)] [[PubMed](#)]
76. Tamburello, G.; Aiuppa, A.; McGonigle, A.J.S.; Allard, P.; Cannata, A.; Giudice, G.; Kantzas, E.P.; Pering, T.D. Periodic volcanic degassing behavior: The Mount Etna example. *Geophys. Res. Lett.* **2013**, *40*, 4818–4822. [[CrossRef](#)]
77. Pering, T.D.; Ilanko, T.; Wilkes, T.C.; England, R.A.; Silcock, S.R.; Stanger, L.R.; Willmott, J.R.; Bryant, R.G.; McGonigle, A.J.S. A Rapidly Convecting Lava Lake at Masaya Volcano, Nicaragua. *Front. Earth Sci.* **2019**, *6*, 241. [[CrossRef](#)]
78. Williams-Jones, G.; Horton, K.A.; Elias, T.; Garbeil, H.; Mouginiis-Mark, P.J.; Sutton, A.J.; Harris, A.J.L. Accurately measuring volcanic plume velocity with multiple UV spectrometers. *Bull. Volcanol.* **2006**, *68*, 328–332. [[CrossRef](#)]
79. McGonigle, A.J.S.; Hilton, D.R.; Fischer, T.P.; Oppenheimer, C. Plume velocity determination for volcanic SO₂ flux measurements. *Geophys. Res. Lett.* **2005**, *32*, 1–4. [[CrossRef](#)]
80. Peters, N.; Hoffmann, A.; Barnie, T.; Herzog, M.; Oppenheimer, C. Use of motion estimation algorithms for improved flux measurements using SO₂ cameras. *J. Volcanol. Geotherm. Res.* **2015**, *300*, 58–69. [[CrossRef](#)]
81. Peters, N.; Oppenheimer, C. Plumetrack: Flux calculation software for UV cameras. *Comput. Geosci.* **2018**, *118*, 86–90. [[CrossRef](#)]

82. Delle Donne, D.; Tamburello, G.; Aiuppa, A.; Bitetto, M.; Lacanna, G.; D'Aleo, R.; Ripepe, M. Exploring the explosive-effusive transition using permanent ultraviolet cameras. *J. Geophys. Res. Solid Earth* **2017**, *122*, 4377–4394. [[CrossRef](#)]
83. Delle Donne, D.; Aiuppa, A.; Bitetto, M.; D'aleo, R.; Coltelli, M.; Coppola, D.; Pecora, E.; Ripepe, M.; Tamburello, G. Changes in SO₂ Flux Regime at Mt. Etna Captured by Automatically Processed Ultraviolet Camera Data. *Remote Sens.* **2019**, *11*, 1201. [[CrossRef](#)]
84. Ilanko, T.; Pering, T.; Wilkes, T.; Apaza Choquehuayta, F.; Kern, C.; Díaz Moreno, A.; de Angelis, S.; Layana, S.; Rojas, F.; Aguilera, F.; et al. Degassing at Sabancaya volcano measured by UV cameras and the NOVAC network. *Volcanica* **2019**, *2*, 239–252. [[CrossRef](#)]
85. Liu, E.J.; Wood, K.; Mason, E.; Edmonds, M.; Aiuppa, A.; Giudice, G.; Bitetto, M.; Francofonte, V.; Burrow, S.; Richardson, T.; et al. Dynamics of Outgassing and Plume Transport Revealed by Proximal Unmanned Aerial System (UAS) Measurements at Volcán Villarrica, Chile. *Geochem. Geophys. Geosyst.* **2019**, *20*, 730–750. [[CrossRef](#)]
86. Gaudin, D.; Moroni, M.; Taddeucci, J.; Scarlato, P.; Shindler, L. Pyroclast Tracking Velocimetry: A particle tracking velocimetry-based tool for the study of Strombolian explosive eruptions. *J. Geophys. Res. Solid Earth* **2014**, *119*, 5369–5383. [[CrossRef](#)]
87. Thielicke, W.; Stamhuis, E.J. PIVlab—Towards User-friendly, Affordable and Accurate Digital Particle Image Velocimetry in MATLAB. *J. Open Res. Softw.* **2014**, *2*. [[CrossRef](#)]
88. Thielicke, W. The flapping Flight of Birds: Analysis and Application. Ph.D. Thesis, University of Groningen, Groningen, The Netherlands, 2014.
89. Campion, R.; Delgado-Granados, H.; Mori, T. Image-based correction of the light dilution effect for SO₂ camera measurements. *J. Volcanol. Geotherm. Res.* **2015**, *300*, 48–57. [[CrossRef](#)]
90. Kern, C.; Werner, C.; Elias, T.; Sutton, A.J.; Lübcke, P. Applying UV cameras for SO₂ detection to distant or optically thick volcanic plumes. *J. Volcanol. Geotherm. Res.* **2013**, *262*, 80–89. [[CrossRef](#)]
91. Lübcke, P.; Bobrowski, N.; Illing, S.; Kern, C.; Alvarez Nieves, J.M.; Vogel, L.; Zielcke, J.; Delgado Granados, H.; Platt, U. On the absolute calibration of SO₂ cameras. *Atmos. Meas. Tech.* **2013**, *6*, 677–696. [[CrossRef](#)]
92. Klein, A.; Lübcke, P.; Bobrowski, N.; Kuhn, J.; Platt, U. Plume propagation direction determination with SO₂ cameras. *Atmos. Meas. Tech.* **2017**, *10*, 979–987. [[CrossRef](#)]
93. Barnie, T.; Bombrun, M.; Burton, M.R.; Harris, A.; Sawyer, G. Quantification of gas and solid emissions during Strombolian explosions using simultaneous sulphur dioxide and infrared camera observations. *J. Volcanol. Geotherm. Res.* **2015**, *300*, 167–174. [[CrossRef](#)]
94. Polacci, M.; Baker, D.R.D.; La Rue, A.; Mancini, L.; Allard, P. Degassing behaviour of vesiculated basaltic magmas: An example from Ambrym volcano, Vanuatu Arc. *J. Volcanol. Geotherm. Res.* **2012**, *233–234*, 55–64. [[CrossRef](#)]

